

Application of a helicity proxy to edge-on galaxies

Axel Brandenburg^{1,2,3,4*} and Ray S. Furuya⁵

¹*Nordita, KTH Royal Institute of Technology and Stockholm University, Roslagstullsbacken 23, SE-10691 Stockholm, Sweden*

²*Department of Astronomy, AlbaNova University Center, Stockholm University, SE-10691 Stockholm, Sweden*

³*JILA and Laboratory for Atmospheric and Space Physics, University of Colorado, Boulder, CO 80303, USA*

⁴*McWilliams Center for Cosmology & Department of Physics, Carnegie Mellon University, Pittsburgh, PA 15213, USA*

⁵*Institute of Liberal Arts and Sciences, Tokushima University, Minami Jousanajima-machi 1-1, Tokushima 770-8502, Japan*

9 April 2020, Revision: 1.113

ABSTRACT

We propose to detect a proxy of the magnetic helicity in galaxies by observing the dust polarization of the edge-on galaxy NGC 891. Our numerical results of mean-field dynamo calculations show that there should be a large-scale component of the rotationally invariant parity-odd B polarization that we predict to be negative in the first and third quadrants, and positive in the second and fourth quadrants. The large-scale parity-even E polarization is predicted to be negative near the axis and positive further away in the outskirts. These properties are shown to be mostly a consequence of the magnetic field being azimuthal and the polarized intensity being maximum at center of the galaxy and not, however, a signature of magnetic helicity.

Key words: dynamo — MHD — polarization — turbulence — galaxies: magnetic fields — galaxies: individual: NGC 891

1 INTRODUCTION

The magnetic fields of spiral galaxies possess a clear large-scale component along with a fluctuating component of comparable strength (Beck et al. 1996; Han 2017). Owing to the presence of turbulence in the interstellar medium (ISM), there is significant turbulent diffusion, which would destroy the large scale magnetic field on a time scale of less than a billion years (Shukurov 1998), unless there is a correspondingly strong anti-diffusive mechanism. The best known mechanism for explaining the origin and maintenance of galactic large-scale magnetic fields is the α effect (Parker 1955; Steenbeck et al. 1966). In the context of galactic dynamo theory, it was first explored by Parker (1971) and Vainshtein & Ruzmaikin (1971). The existence of the α effect requires a violation of statistical mirror symmetry, which implies the presence of magnetic helicity. It is crucial to assess the validity of the dynamo models toward a more comprehensive understanding of how a galaxy forms its structure and how magnetic fields regulate the cycle of the ISM by enhancing and suppressing star-formation activity in a galaxy. However, there is no explicit evidence that the α effect really does operate in galaxies.

Methods for measuring the helicity of the magnetic field in our Galaxy and in distant galaxies have been proposed on several occasions in recent years (Volegova & Stepanov 2010; Junklewitz & Enßlin 2011; Oppermann et al. 2011;

Brandenburg & Stepanov 2014; Horellou & Fletcher 2014). Measuring this for edge-on galaxies may be particularly advantageous, because we can then see both the upper and lower disc planes simultaneously. However, to measure the magnetic helicity, one needs the full magnetic field vector, but the linear polarization parameters Stokes, Q and U , only allow one to determine the magnetic field direction up to a 180° ambiguity. For this reason it is preferable to work directly with the Stokes parameters and to determine from them a helicity proxy. The quantity of interest is then the parity-odd contribution to the rotationally invariant constituent of the linear polarization, or possibly the correlation between the parity-even and parity-odd polarizations (Kamionkowski et al. 1997; Seljak & Zaldarriaga 1997). This is a relatively new technique, which has recently been applied to the Sun’s magnetic field (Brandenburg et al. 2019, hereafter BBKMRPS); see also Brandenburg (2019) and Prabhu et al. (2020), and Kahniashvili et al. (2014) for the original motivation in the cosmological context.

The attributes parity-even and parity-odd mean the same as mirror-symmetric and mirror-antisymmetric—at least in a statistical sense. For example, a cyclone on a weather map is not statistically mirror-symmetric. In fact, a cyclone in the Northern hemisphere looks like a mirror image of a cyclone in the Southern hemisphere. A cyclone is therefore statistically mirror antisymmetric. The underlying physical quantity is the kinematic helicity. It is a pseudoscalar, because it changes sign when the system is viewed

* E-mail: brandenb@nordita.org

through a mirror or under parity transformation. The pressure, by contrast, is a scalar; it behaves similarly in the

In dynamo theory, one sometimes characterizes the magnetic field as even or odd about the equator. As a continuous measure of the type and degree of symmetry, one defines the ratio of the difference of the energies contained in the symmetric and antisymmetric parts, divided by their sum. This quantity is sometimes also called parity (Brandenburg et al. 1989), but it is not a pseudoscalar and is therefore, in this sense, a misnomer.

Before we define the parity-even and parity-odd constituents of linear polarization, let us emphasize that these quantities are, at best, a proxy of magnetic helicity. As was already demonstrated in BBKMRPS and Bracco et al. (2019), there cannot be a detailed correspondence with helicity, because polarization is only defined with respect to a plane. If the velocity or magnetic field are statistically isotropic, these fields can still be fully helical (Moffatt 1978), but a planar image of a cyclone could, with equal probability, also be seen from its back side, so it would appear like its mirror image. Of course, turbulence in galaxies is inhomogeneous, i.e., its statistical properties are not the same in different places. An observer can tell whether one is observing from the outside or the inside. Therefore, there is a chance (but no guarantee) that a particular polarization pattern is preferred over its mirror image. Rotating convection, inspected from the top surface, is such an example in the context of solar turbulence. The magnetic field in our Galaxy is another example (Brandenburg & Brüggén 2020, hereafter BB20).

Let us emphasize at this point that the use of the parity-odd constituent of linear polarization as a proxy of magnetic helicity does not explicitly require information about the line-of-sight component of the magnetic field. Faraday rotation measurements are therefore not invoked in our study. As was already discussed in Brandenburg (2019), this can be regarded as a disadvantage, but we have to keep in mind that our technique is not trying to reconstruct the magnetic field. Instead, we use the appropriate and complete description of linear polarization to obtain a pseudoscalar without the need for a questionable reconstruction. It is simply a new diagnostic and it is then up to us to find out whether or not it has anything to do with magnetic helicity. It might also have to do with differential rotation, or with a combination of helicity and differential rotation.

The purpose of the present work is to learn more about the theoretically expected patterns for edge-on galaxies by taking NGC 891 as a representative case. Here, we consider a numerical solution of a simple galactic mean-field dynamo of $\alpha\Omega$ type. The magnetic field is generated by the α effect (Krause & Rädler 1980) and differential rotation. We embed a flat dynamo in a Cartesian domain. We do this by choosing a distribution of α that is concentrated about the midplane and has opposite signs above and below it. The magnetic diffusivity is taken to be constant. The radius of the disc is assumed to be 15 kpc. Some of our models are similar to those of Brandenburg et al. (1993), who discussed the application to two particular edge-on galaxies, NGC 891 and NGC 4631. Recent multi-wavelength continuum emission studies between wavelengths of 3.6 μm and 2.6 mm clearly show that the properties of dust grains in the ISM of NGC 891 are similar to those in the Milky Way

(Hughes et al. 2014). This makes this galaxy an ideal laboratory for testing not only our model, but also for studying the roles of magnetic fields in galaxies in general.

At this point, our goal is to identify characteristic and distinguishing features in the polarization pattern rather than to construct a detailed prediction for NGC 891, which would include a detailed treatment of the wind, as was done in Brandenburg et al. (1993), and more recently by Moss & Sokoloff (2017). The wind can both enhance and suppresses dynamo action (Chamandy et al. 2015). Most importantly, however, it can make the polarization segments more radial and thus closer to what is observed (Elstner et al. 1995). There is also great interest in modeling the magnetic field in the galactic halo (Sokoloff & Shukurov 1990; Brandenburg et al. 1992), where significant magnetic field strengths are observed (Krause 2015).

2 PARITY-EVEN AND PARITY-ODD POLARIZATIONS

In the context of polarimetry of the cosmic microwave background radiation, one commonly decomposes the linear polarization into the parity-even E and the parity-odd B polarizations. They are defined in terms of a global expansion on the full sphere of the sky. Here, however, we are only interested in local Cartesian patches in the sky. We can then employ standard Fourier transformation of the complex polarization $P = Q + iU$ to compute the quantity

$$\tilde{R}(k_x, k_z) = (\hat{k}_x - i\hat{k}_z)^2 \int e^{-i\mathbf{k}\cdot\mathbf{x}} P(\mathbf{x}) d^2\mathbf{x}, \quad (1)$$

where a tilde indicates Fourier transformation of a quantity R over the spatial coordinates in the projected plane in the sky, which are here the x and z coordinates. The real and imaginary parts of R give the E and B polarizations, and \hat{k}_x and \hat{k}_z are the x and z components of the planar unit vector $\hat{\mathbf{k}} = \mathbf{k}/k$, with $\mathbf{k} = (k_x, k_z)$ and $k = (k_x^2 + k_z^2)^{1/2}$ being the length of \mathbf{k} . Thus, we have

$$E(\mathbf{x}) + iB(\mathbf{x}) \equiv R = \int e^{i\mathbf{k}\cdot\mathbf{x}} \tilde{R}(\mathbf{k}) d^2\mathbf{k}/(2\pi)^2. \quad (2)$$

The occurrence of the factor $(\hat{k}_x - i\hat{k}_z)^2$ in Eq. (1) is explained by the fact that it is the square of the complex conjugate of the generating function $\hat{k}_x + i\hat{k}_z$ for pure E and B modes. Multiplying this by a phase factor $e^{i\pi n/4}$ samples E patterns for $n = 0$ and 2 and B patterns for $n = 1$ and 3 in a continuous fashion (Brandenburg 2020); see also standard text books in the field (Durrer 2008) and reviews Kamionkowski & Kovetz (2016).

When comparing the signs of E and B with other work in the literature, one should be aware of the possibility of different conventions; see Brandenburg (2019) and Prabhu et al. (2020) for a more detailed discussion. We refer to Appendix A for a comparison relevant to the present work.

The E polarization corresponds to cross-like magnetic field patterns if $E > 0$ and to ring-like magnetic field patterns if $E < 0$. Positive (negative) B polarizations, on the other hand, correspond to clockwise (counterclockwise) inward spiraling patterns. The latter pattern is evidently parity-odd, because that for $B > 0$ becomes the pattern for

Table 1. Signs of E and B reported in the literature for characteristic features in various cases and viewing directions.

case	E	B	view	reference
rotating convection	–	–	face-on	BBKMRPS
solar active regions	–	+	face-on	Prabhu et al. (2020)
Galaxy	–	+	Sun	BB20
spherical dynamo	–	–	edge-on	Brandenburg (2019)
edge-on galaxies	–	–	edge-on	present work

$B < 0$ under parity transformation. By contrast, the E patterns do not change under parity transformation. In this paper, we consider an edge-on galaxy, so we are not concerned with the grand spiral design of galaxies. This, too, could in principle lead to B polarization, but this would require the galaxy to be viewed face-on.

Even when the system is inhomogenous and a finite B emerges, it is not yet clear what its sign is. This uncertainty may be mainly due to the fact that the B polarization has not yet been studied under sufficiently many circumstances. It does depend on the spatial magnetic field pattern produced by the system. The experience gathered so far is somewhat sketchy; see Table 1 for a summary. The results depend not only on the nature of the physical system under consideration, but also on the viewing direction. Viewing a disk galaxy from the outside, for example edge-on, will produce the opposite result for the B polarization as viewing from the inside, for example when viewing our Galaxy from the position of the Sun, as was done by BB20.

Looking at Table 1, there seems to be agreement regarding a negative sign for E , but B can have either sign, depending on circumstances. In rotating convection, $E < 0$ and $B < 0$; see Fig. 10 of BBKMRPS. In solar active regions; $E < 0$ but $B > 0$; see Fig. 5 of Prabhu et al. (2020). Also near the Galactic midplane, $E < 0$ and $B > 0$ (BB20). For a spherical mean-field dynamo, Fig. 1 of Brandenburg (2019) shows positive E and B in the North, but this corresponds to $E < 0$ and $B < 0$. This would agree with the present paper if we took E near the axis and B in the first and third quadrants in an edge-on view. We emphasize again that these properties with respect to North and South are independent of the question of whether the magnetic field is even or odd about the equatorial plane. Determining this with Faraday rotation measurements is certainly of interest, but it is not explicitly connected with our helicity proxy.

3 THE MODEL

We adopt the galactic dynamo model of Brandenburg (2015). It is fully three-dimensional, but when computing an edge-on view, we consider a specific xz cross-section through $y = -10$ kpc viewed from the direction $y \rightarrow -\infty$; see Fig. 1. We chose the slice $y = -10$ kpc as a compromise that is well before the central slice through $y = 0$ and already sufficiently far into the galaxy to be representative of its field near its periphery. We compute the complex polarization, $P = Q + iU$, as

$$P = -\epsilon (b_x + ib_z)^2 / \mathbf{b}_\perp^2, \quad (3)$$

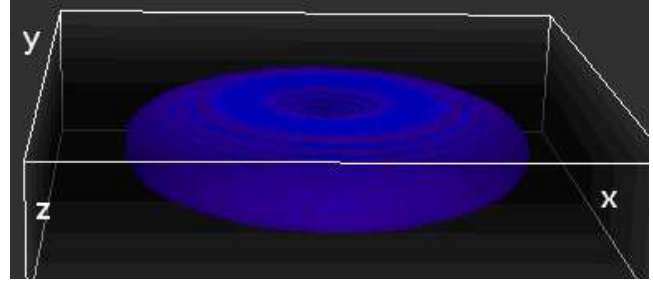


Figure 1. Three-dimensional visualization of B^2 for Model B. The nearly edge-on observer sees the xz plane and is located in the negative y direction.

where $\mathbf{b}_\perp \equiv (b_x, b_z)$ is the magnetic field vector in the (x, z) plane and ϵ is the emissivity (Alton et al. 2004; Planck Collaboration Int. XIX 2015), which is here assumed to be constant. The viewing direction is from $y \rightarrow -\infty$, which is consistent with the viewing direction $z \rightarrow \infty$ of (b_x, b_y) , which was applied in rotating convection and inspections of the Sun (BBKMRPS). Next, we compute $R = E + iB$ using Eq. (2). We then show $E(x, z)$ and $B(x, z)$ at a given position y ; see Figs. 2 and 3.

We adopt a mean-field model where all dependent variables are defined as azimuthal averages indicated by an overbar. The mean magnetic field $\overline{\mathbf{B}}$ is expressed in terms of the mean magnetic vector potential $\overline{\mathbf{A}}$ as $\overline{\mathbf{B}} = \nabla \times \overline{\mathbf{A}}$. We solve the $\alpha\Omega$ dynamo equation in its simplest form,

$$\frac{\partial \overline{\mathbf{A}}}{\partial t} = \overline{\mathbf{U}} \times \overline{\mathbf{B}} + \alpha \cdot \overline{\mathbf{B}} - \eta_T \mu_0 \overline{\mathbf{J}}, \quad (4)$$

where $\overline{\mathbf{U}}$ is the mean flow, $\overline{\mathbf{J}} = \nabla \times \overline{\mathbf{B}} / \mu_0$ is the mean current density, μ_0 is the vacuum permeability, $\alpha = \text{diag}(\alpha_\perp, \alpha_\perp, 0)$ is the α tensor in the limit of rapid rotation (Rüdiger 1978), and η_T is the total (microphysical and turbulent) magnetic diffusivity. The mean flow is composed of toroidal and poloidal components, $\overline{\mathbf{U}}_t$ and $\overline{\mathbf{U}}_p$, respectively, describing the galactic rotation profile and a galactic wind.

In the following we assume the galactic rotation to be represented by a modified Brandt rotation profile of the form $\overline{\mathbf{U}}_t = \varpi \Omega(\varpi)$, where $\varpi = (x, y, 0)$ with $\varpi = |\varpi|$ being the cylindrical radius, and

$$\Omega = \Omega_0 / [1 + (\varpi / \varpi_\Omega)^n]^{1/n} \quad (5)$$

is the angular velocity with $\Omega_0 = \text{const}$ characterizing the rigid rotation law for $\varpi < \varpi_\Omega$, and $\varpi_\Omega = 3$ kpc is the radius where the rotation law attains constant linear velocity $V_0 = \Omega_0 \varpi_\Omega$. The exponent $n = 4$ has been chosen to make the transition from rigid to constant rotation sharp. This is not very important and, in hindsight, could have been avoided.

For the α effect we assume a nonlinear (α -quenched) formulation (Ivanova & Ruzmaikin 2008) for the horizontal components of the α tensor and choose

$$\alpha_\perp = \frac{\alpha_0}{1 + Q_\alpha \overline{\mathbf{B}}^2 / B_{\text{eq}}^2} \frac{z}{H_\alpha} \exp\left(-\frac{z^2}{H_\alpha^2}\right) f_\alpha(\varpi) g_\alpha(\varpi), \quad (6)$$

where H_α is the disc height for the α effect, α_0 quantifies its strength, and $f_\alpha(\varpi)$ and $g_\alpha(\varpi)$ are radial profiles that we apply in Model B. In those cases, we use

$$f_\alpha(\varpi) = [1 - \text{erf}(\varpi / \varpi_\alpha)] / 2 \quad (7)$$

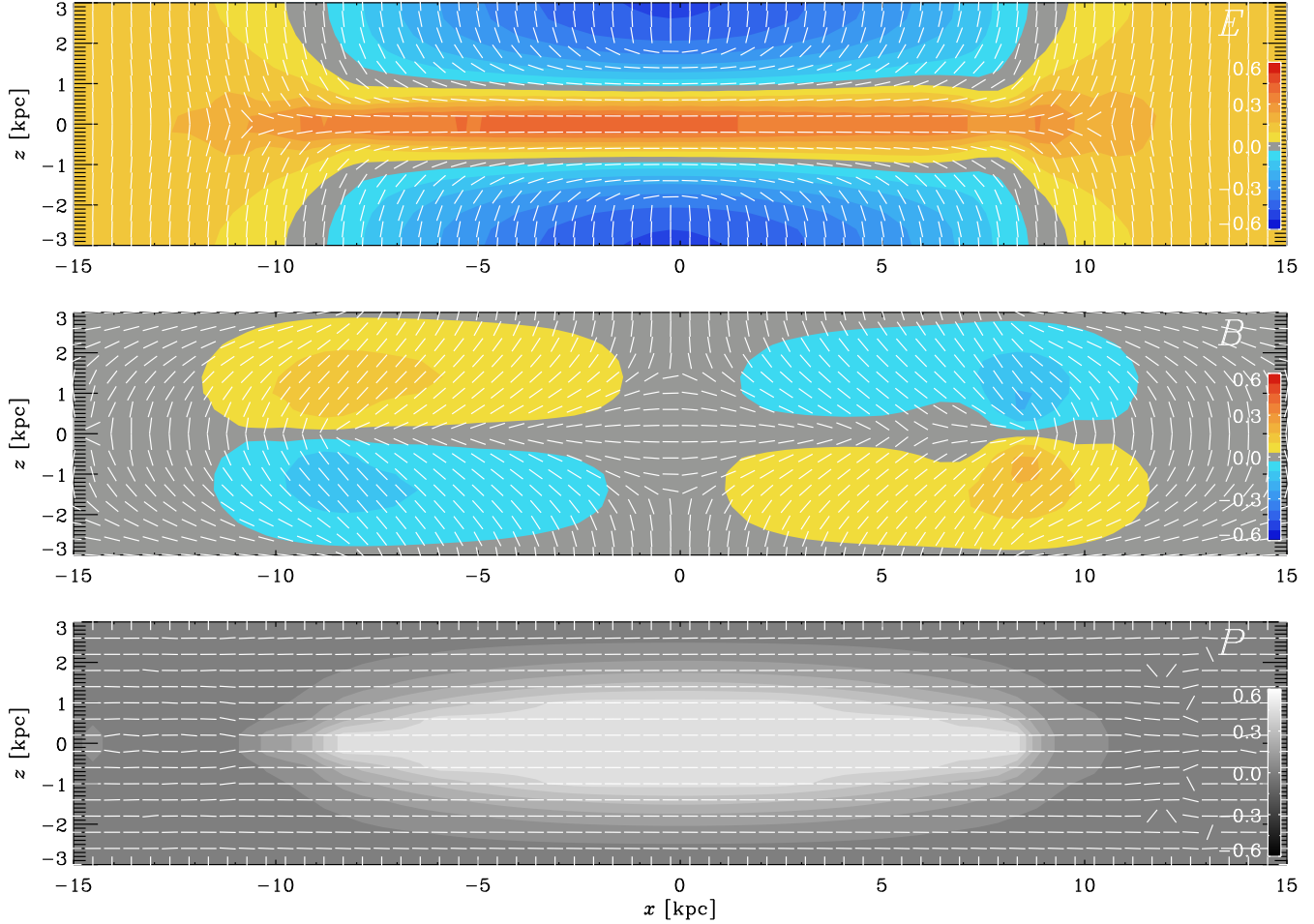


Figure 2. E and B polarizations in an edge-on view of Model A, which is the galactic dynamo model of Brandenburg (2015). The polarization segments show separately the directions of the E and B polarizations, and the color scale shows the values of E and B in units where $\epsilon = 1$ in Eq. (3); see (BBKMRPS).

to introduce a radial cutoff at $\varpi = \varpi_\alpha = 15$ kpc, and

$$g_\alpha(\varpi) = [1 + (\varpi/\varpi_{\alpha\Omega})^n]^{-1/n} \quad (8)$$

to allow for an additional radial modulation with $\varpi_{\alpha\Omega} = \varpi_\Omega$ in Model B, such that α_\perp is proportional to the local angular velocity, as was assumed in the model of Brandenburg et al. (1993), who assumed $\alpha_0 = \Omega_0 \ell$, with $\ell = 0.3$ kpc being the correlation length. In Model A, on the other hand, α_\perp is independent of ϖ and therefore we put $\varpi_{\alpha\Omega} = \infty$. Note that in both cases, owing to the z/H_α factor in front of the exponential function, α_\perp changes sign about the midplane. This reflects the opposite orientation of the Coriolis force on the two sides of the midplane.

We also define the equipartition field strength as $B_{\text{eq}} = \sqrt{\mu_0 \rho} u_{\text{rms}}$, where u_{rms} is the root-mean-square value of the turbulent velocity; see also Eq. (1) of Beck et al. (2019). Using $u_{\text{rms}} = 10 \text{ km s}^{-1}$ and $\rho = 2 \times 10^{-24} \text{ g cm}^{-3}$, we have $B_{\text{eq}} = 5 \mu\text{G}$ (Brandenburg et al. 1993), which is the value we use in all of our models. Note that the line-of-sight and plane-of-sky components of the magnetic field toward galactic molecular clouds are on the order of 1–100 μG , estimated from Zeeman effect measurements (e.g., Crutcher 2012) and dust polarization studies (e.g., Pattle & Fissel 2019), respec-

tively. The parameter Q_α is a nondimensional constant that determines the strength of α -quenching, and thereby the overall magnetic field strength. We choose $Q_\alpha = 25$, so the resulting mean magnetic field strength attains plausible values of somewhat below 10 μG .

On the periphery of the computational domain, we assume normal-field conditions, i.e., $\hat{\mathbf{n}} \cdot \bar{\mathbf{A}} = (\hat{\mathbf{n}} \cdot \nabla) \times \bar{\mathbf{A}} = 0$, where $\hat{\mathbf{n}}$ is the unit vector normal to the boundary. The initial condition for $\bar{\mathbf{A}}(\mathbf{x}, 0)$ is Gaussian distributed white noise of low amplitude. In this paper, we measure lengths in kpc and speeds in km s^{-1} , so time is measured in units of 0.98 Gyr. For simplicity, we drop the factor 0.98 when specifying times or inverse times.

We consider two models. First, we take the one of Brandenburg (2015), which was designed to reflect typical spiral galaxies. Second, we modify the parameters (rotation curve and α effect) such that they match those of the model of Brandenburg et al. (1993) of NGC 891. In both cases, we use $64^2 \times 16$ mesh points, which proved sufficient to resolve the spatial structure of the magnetic field. Calculations with $128^2 \times 32$ mesh points produced virtually identical polarization maps. To demonstrate the usefulness of our diagnostic as a proxy for magnetic helicity in terms of the B polar-

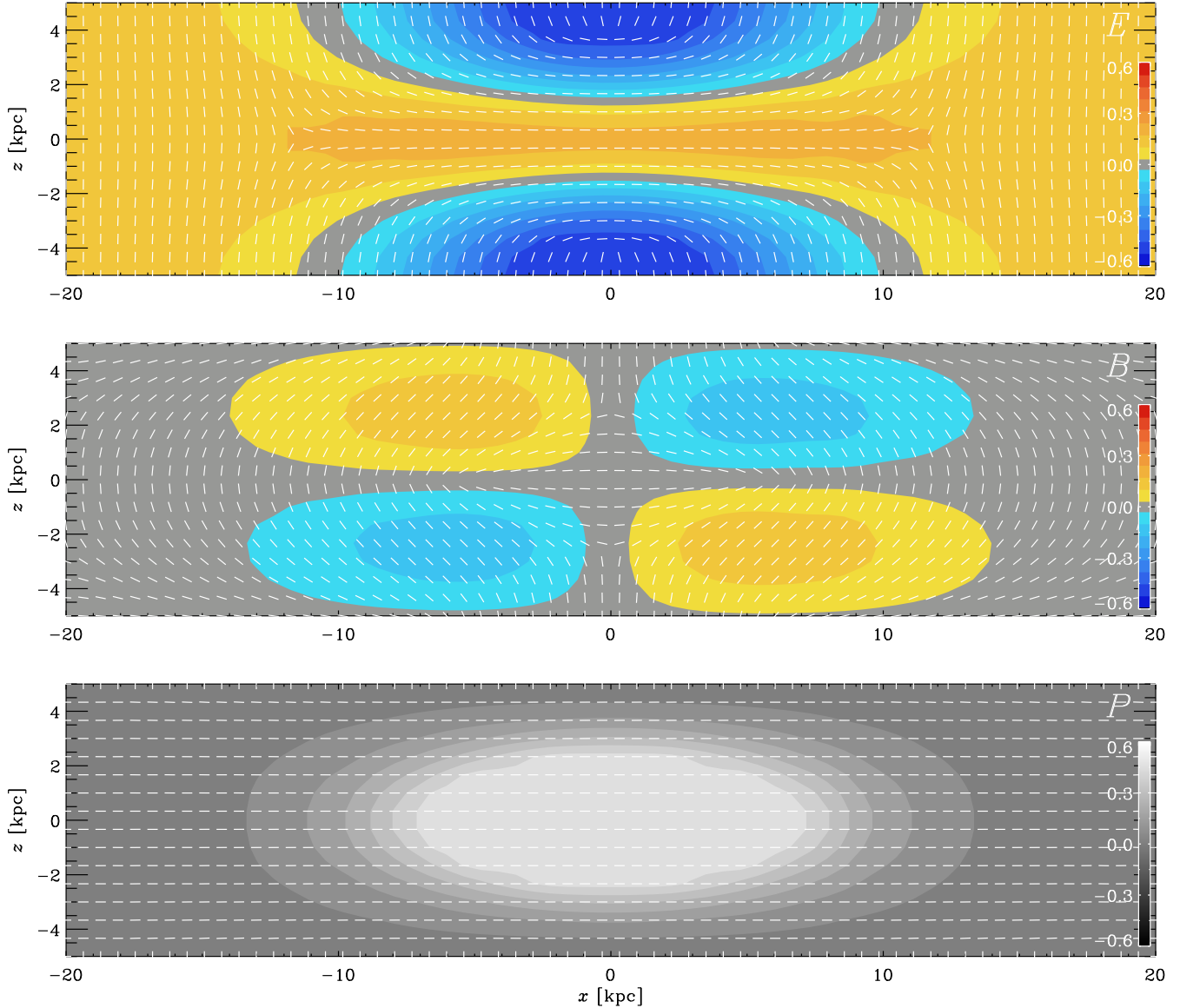


Figure 3. Same as Fig. 2, but for Model B with parameters relevant to NGC 891. Note the pixel resolution of about 650 pc, which corresponds to the 14 arcsecond beam of the JCMT at $850\ \mu\text{m}$ wavelength.

ization, we also present a model with a negative α_0 , where we expect the sign of the magnetic helicity to be reversed relative to what it is otherwise. However, the nature of the $\alpha\Omega$ dynamo also changes and the most easily excited field is then an oscillatory one, so no direct comparison is possible.

The computations are performed with the PENCIL CODE (Brandenburg & Dobler 2010). We emphasize in this connection that we are dealing here with a mean field model, so no sharp structures are expected to occur in such a case. In Table 2 we summarize the various parameters used here. We also give the instantaneous growth rate $\lambda = d \ln B_{\text{rms}}/dt$ during the early exponential growth phase. For the oscillatory Model C, however, we give λ as a complex number, where the real part indicates the growth rate averaged over one period P and the imaginary part indicates the frequency $2\pi/P$.

Table 2. Parameters of the dynamo models discussed.

	Ω_0 [Gyr $^{-1}$]	ϖ_Ω [kpc]	α_0 [km s $^{-1}$]	H_α [kpc]	ϖ_α [kpc]	$\varpi_{\alpha\Omega}$	λ [Gyr $^{-1}$]
A	100	3	16	0.2	—	∞	10
B	75	3	22	1.5	15	ϖ_Ω	10
C	75	3	-15	1.5	15	ϖ_Ω	$2.5 + 0.88i$

4 RESULTS

4.1 E and B polarizations

Our models lead to an early exponential growth of the magnetic field and reach saturation after about 10 Gyr. Here we consider only the saturated phase of the models. As a first

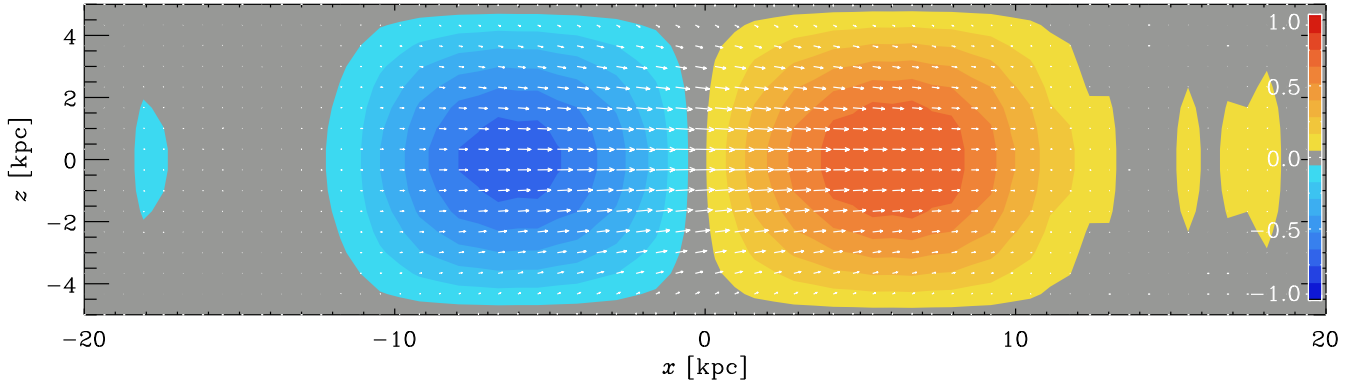


Figure 4. Visualization of the magnetic field for Model B in the same slice for which E and B are shown in Fig. 3. Here, b_z has been scaled by a factor of 20 relative to b_x , but the vertical field still seems almost completely negligible.

step, we show in Fig. 2 the E and B polarizations together with the polarized intensity and polarization segments for Model A from the xz plane near $y = -10$ kpc. In Fig. 3 we again show the E and B polarizations, but now for Model B. The polarized intensity and polarization segments show just a horizontal pattern. It is therefore amazing that the decomposition into its rotationally invariant constituents appears so much richer. The primary reason for this is connected just with the spatial variation of the polarized intensity. This is demonstrated in Appendix A, where we show the E and B polarizations for a polarization signal where Stokes $U = 0$ and Stokes Q consists of just a Gaussian.

There are remarkable similarities between the polarization patterns obtained from a Gaussian and those obtained from our dynamo model. This suggests that the information content in the overall pattern seen in Figs. 2 and 3 is not very profound, although more physically meaningful information may still be hidden within the more subtle departures from this overall pattern.

The pixel resolution in Fig. 3 is about 650 pc, which is the spatial resolution when NGC 891 is observed at a distance of 9.6 Mpc (Strickland et al. 2004) with the 14 arcsecond beam of the JCMT at $850 \mu\text{m}$ wavelength. We see that, in both cases, E is symmetric about the midplane $z = 0$, and B is antisymmetric. Moreover, E is negative in the halo near the axis ($x = 0$) and positive near the midplane further away from the axis. In Model A, however, E is positive at the center ($x = z = 0$), while in Model B it is negative at $x = z = 0$. As expected, B changes sign about the equator. It also changes sign between the two sides of the rotation axis. In the first and third quadrants, the sign is negative, while in the second and fourth, it is positive. The arrow-less vectors or polarization segments of the B polarization show a clockwise inward swirl in the first and third quadrants and an anti-clockwise inward swirl in the second and fourth quadrants. This signature seems to be surprisingly independent of the differences between Models A and B. The patterns of E and B are also rather smooth; the typical scale would be the scale height of the magnetic field, which is about 2 kpc. In this context, we must recall that our model can only deliver the mean magnetic field, and that the actual magnetic field must also contain a fluctuating component of smaller scales below 100 pc.

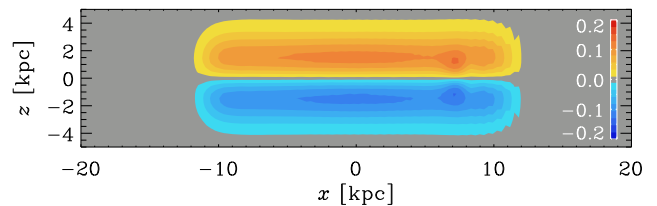


Figure 5. Visualization of the normalized current helicity density, $\mu_0 \overline{\mathbf{J} \cdot \mathbf{B}}$, for Model B at $y = -10$ kpc.

4.2 Magnetic field and helicity

It is important to realize that neither the helicity of the magnetic field nor any proxy of it can easily be discerned from just a simple inspection of the magnetic field. This is mostly because of the strong dominance of the azimuthal magnetic field over the vertical field. This becomes clear once again from Fig. 4, where we show vectors of \mathbf{b}_\perp superimposed on a color scale representation of b_y . Here, b_z has been scaled by a factor of 20 relative to b_x , but the vertical field still seems almost completely negligible.

It is long known that the magnetic field in galaxies tends to have even symmetry about the equatorial plane. This is also the case for all of our models. This means that the azimuthal magnetic field is symmetric about the midplane and the vertical magnetic field is antisymmetric about in the midplane, just as seen from Fig. 4. Note, also, that the strongest magnetic field occurs at a distance of about 7 kpc from the center. The results for Model A are similar, except that here the strongest magnetic field occurs at a distance of about 5 kpc from the center.

To make contact with the helicity of the magnetic field in our model, we plot in Fig. 5 a vertical slice of the current helicity density $\overline{\mathbf{J} \cdot \mathbf{B}}$. We can see that $\overline{\mathbf{J} \cdot \mathbf{B}}$ is mostly positive (negative) in the upper (lower) disc plane. This agrees with the sign of α_\perp , which is also positive (negative) in the upper (lower) disc plane. For $Q_\alpha = 25$, the normalized current helicity density, $\mu_0 \overline{\mathbf{J} \cdot \mathbf{B}}$, would be units of $\mu\text{G}^2 \text{kpc}^{-1}$.

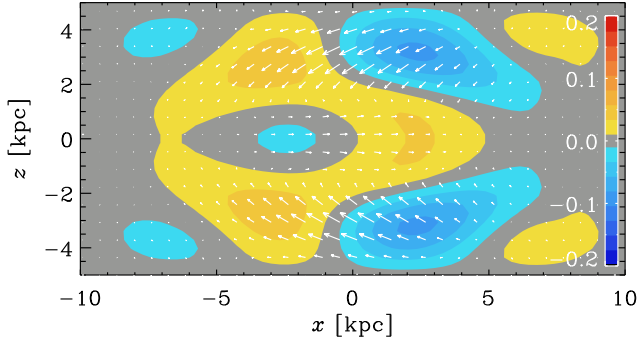


Figure 6. Visualization of the magnetic field, similar to Fig. 4, but for Model C, at $y = -10$ kpc, and b_z has been scaled by a factor of 5 relative to b_x . The plot range in the x direction has been clipped to ± 10 kpc.

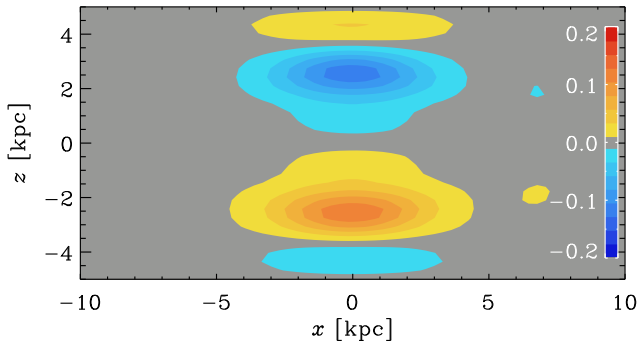


Figure 7. $\mu_0 \overline{\mathbf{J} \cdot \mathbf{B}}$, similar to Fig. 5, but for Model C, and again at $y = -10$ kpc.

4.3 Negative α and reversed helicity

To give a sense of the range of possibilities for the E and B patterns in models of edge-on galaxies, we now consider Model C with a negative α_0 . As mentioned in Sect. 3, such a model is not exactly a mirror image of a model with a positive value of α_0 , because the nature of the dynamo also changes. In the present case, the field becomes oscillatory, but retains its even symmetry with respect to the midplane; see Fig. 6 for a visualization of the magnetic field in a cross-section through $y = -10$ kpc. Note that the magnetic field is fairly much confined within a cylindrical radius of 10 kpc. This is why we have clipped in Fig. 6 (and the following two figures) the x range beyond ± 10 kpc. However, the numerical calculations have been carried out, just as before, in the larger domain with $|x|, |y| \leq 20$ kpc.

To verify that the magnetic helicity has indeed changed sign, we show in Fig. 7 the current helicity, again through the plane $y = -10$ kpc. We see that $\overline{\mathbf{J} \cdot \mathbf{B}}$ is now indeed negative in the upper disc plane, but there is an additional sign change close to the vertical boundaries.

Finally, the resulting E and B polarizations at $y = -10$ kpc are shown in Fig. 8. Note that B has changed sign with respect to Figs. 2 and 3, at least sufficiently close to the midplane. Closer to the boundaries at $z = \pm 5$ kpc, this sign has changed again, somewhat similarly to what was seen in Fig. 7 for $\overline{\mathbf{J} \cdot \mathbf{B}}$. The E polarization is somewhat different than before, although the basic features are unchanged:

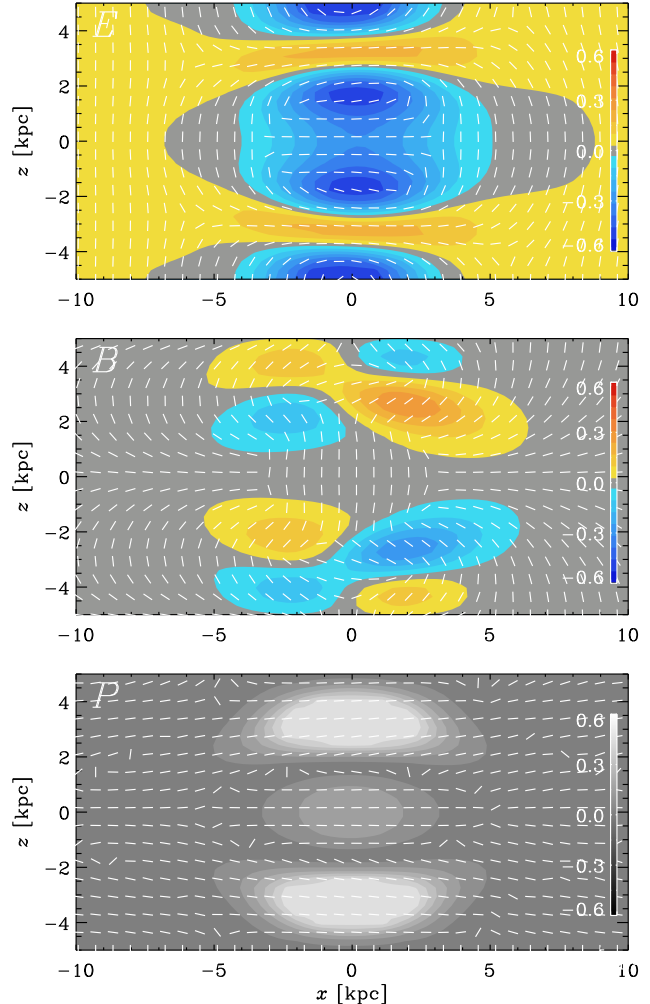


Figure 8. Same as Fig. 2, but for Model C with negative α_0 at an arbitrarily chosen time. The plot range in the x direction has been clipped to ± 10 kpc.

it is negative near the axis and positive further away from it, except right at the midplane. Within the midplane, the negative sign of E near the axis extends now also to larger radii.

Unlike Fig. 3, the polarized intensity now shows concentrations a certain distance away from the midplane. The polarization segments are still mostly horizontal, so the basic phenomenology explained in Appendix A still applies. This explains then why the E and B polarizations in Fig. 7 show a doubling of the features seen in Fig. 3.

5 DISCUSSION AND FUTURE PROSPECTS

Edge-on galaxies provide an opportunity to study some basic aspects of magnetic fields in galaxies. This can have implications for the dynamo interpretation of their generation. Our preliminary investigation suggests that the E polarization is positive near the disc midplane and away from the axis, where it tends to outline star-like patterns in the magnetic field, while in the halo near the axis it is negative, corresponding to ring-like patterns in the magnetic field; see the

top panel of Fig. 2. The B polarization is negative in the first and third quadrants and outlines counterclockwise inward spiraling patterns, while in the second and fourth quadrants, we have positive values, corresponding to clockwise inward spiraling patterns; see the bottom panel of Fig. 2. Again, we emphasize here that our discussion of spiraling polarization patterns concerns the edge-on view of the B polarization and is not connected with the spiraling appearance of galaxies viewed face-on.

Our hope is that the predictions for the signs of the E and B polarizations could soon be verified observationally using observations of dust polarization. Dust polarization observations have proven to be an excellent tool to measure the orientation of the magnetic field in star-forming regions and to assess the relative magnitudes of the mean and turbulent components of the field (Hildebrand et al. 2009). Linear polarization imaging provide the orientation of the plane-of-sky magnetic field lines, as non-spherical dust grains tend to align with their short axis perpendicular to the direction of the magnetic field, giving rise to linear polarization of the emission (Andersson et al. 2015). All-sky dust polarization imaging by *Planck* at $850\ \mu\text{m}$ have revealed well-defined magnetic field patterns in the ISM from Galactic scales down to molecular cloud scales of $\gtrsim 10\ \text{pc}$.

Although a size of $\gtrsim 10\ \text{pc}$ is still one or two orders of magnitude larger than that of dense cloud cores where stars and stellar cluster form, it is worth attempting to investigate the magnetic-field structure with linear polarization imaging at submillimeter (submm) wavelengths. Submm emission polarimetry is sensitive to tracing the column density of the cold ($T \lesssim$ a few times 10 K) ISM, whereas near-infrared (NIR) absorption polarimetry may have suffered from scattering, while cm-wavelength radio polarimetry may have suffered from Faraday rotation. Indeed, recent polarization observations with SOFIA HAWC+ of M 82 and NGC 253 at 53 and $154\ \mu\text{m}$ (Jones et al. 2019) clearly demonstrated such an advantage of submm/FIR polarimetry. Moreover, we point out that previous Herschel PACS and SPIRE imaging at 100, 160, and $250\ \mu\text{m}$ revealed that NGC 891 is rich in dust grains—even toward its halo; the scale height of the dusty halo is $1.44 \pm 0.12\ \text{kpc}$ (Bocchio et al. 2016). We therefore argue that the proposed method in this work is complementary to the conventional two methods (radio synchrotron and NIR polarimetry).

At wavelengths of $850\ \mu\text{m}$, the optical depth is shorter and Faraday rotation effects from the superposition along the line-of-sight are limited (Hughes et al. 2014). Intensity maps of NGC 891 at $850\ \mu\text{m}$ show two “blobs” or “knots” at a distance of about 4–5 kpc from the center (Haas et al. 2002; Whaley et al. 2009). This could also be suggestive of a ring-like magnetic field, similarly to what is seen in Fig. 4. This would be analogous to the ring-like magnetic field of M 31 (Beck et al. 2020). Interestingly, the ring-like concentration cannot easily be explained with kinematic theory (Ruzmaikin et al. 1988), unless one invokes a similar variation of the gas density and thereby of B_{eq} (Beck et al. 1996). Such details have been ignored in our present modeling.

A potential shortcoming of the present calculations is that our predictions are based solely on mean-field dynamos. This means that we only take the large-scale component of the magnetic field into account. In reality, there is also a small-scale component whose helicity is expected to have the

opposite sign (Blackman & Brandenburg 2003). How this affects the detection prospects of systematic E and B polarizations is currently unknown and must be a target of future investigations. The typical scale of fluctuations would not exceed 100 pc (Beck et al. 1996), which is well below the resolution scale of the James Clerk Maxwell Telescope. It is therefore possible that our present results may already give a good hint at what can be observed in the near future. Higher resolution observations would be of great interest for testing the idea of a magnetic helicity reversal at smaller length scales. In the meantime, however, it would be worthwhile to explore this regime of smaller length scales with detailed turbulence simulations without adopting mean field theory.

Another opportunity for improvements is given by our increased knowledge of the rotation curves of NGC 891 (Fraternali et al. 2011). In particular, it is now known that the rotation in the halo of NGC 891 is slower than that in the galactic disc (Oosterloo et al. 2007). This implies the presence of vertical shear that could modify the vertical helicity profile of the galaxy.

ACKNOWLEDGEMENTS

This work was supported in part through the Swedish Research Council, grant 2019-04234, and the National Science Foundation under the grant AAG-1615100. This research is partially supported by Grants-in-Aid for Scientific Researches from the Japan Society for Promotion of Science (KAKENHI 19H0193810). We acknowledge the allocation of computing resources provided by the Swedish National Allocations Committee at the Center for Parallel Computers at the Royal Institute of Technology in Stockholm.

APPENDIX A: E AND B FROM A PATCH IN Q

The purpose of this appendix is to compute the E and B polarization patterns for a signal with Stokes $U = 0$ and Stokes Q consisting of just a Gaussian patch. To also illuminate the question about different sign conventions, we use this opportunity to compare the local approach given by Eqs. (1) and (2) with the global one, where the complex polarization is expanded in terms of spin-2 spherical harmonic functions (e.g., Durrer 2008). We therefore work with spherical coordinates (θ, ϕ) , where θ is colatitude and ϕ is longitude with $0 < \theta < \pi$ and $0 < \phi < 2\pi$. We write Stokes Q in the form

$$Q = Q_0 \exp \left\{ - \left[(\theta - \theta_0)^2 + (\phi - \phi_0)^2 \right] / 2\sigma^2 \right\}, \quad (\text{A1})$$

where we choose $\theta_0 = \phi_0 = \pi/2$ to be a point on the equator and $\sigma = 10^\circ$ is chosen for the size of the patch. The global representations of E and B (indicated by subscripts ‘glob’) are expressed through the complex function

$$E_{\text{glob}} + iB_{\text{glob}} \equiv R = \sum_{\ell=2}^{N_\ell} \sum_{m=-\ell}^{\ell} \tilde{R}_{\ell m} Y_{\ell m}(\theta, \phi), \quad (\text{A2})$$

where the coefficients $\tilde{R}_{\ell m}$ are given by

$$\tilde{R}_{\ell m} = \int_{4\pi} (Q + iU) {}_2Y_{\ell m}^*(\theta, \phi) \sin \theta \, d\theta \, d\phi. \quad (\text{A3})$$

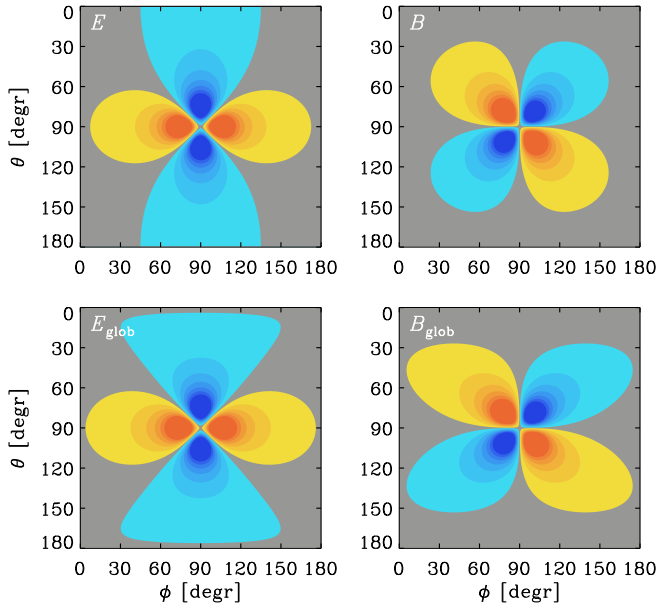


Figure A1. Local representations E and B together with their global counterparts E_{glob} and B_{glob} for a Gaussian patch with just a Stokes Q profile.

Here ${}_2Y_{\ell m}^*(\theta, \phi)$ are the spin-2 spherical harmonics of spherical harmonic degree ℓ and order m and the asterisk denotes complex conjugation. In the cosmological context, both E_{glob} and B_{glob} are defined with a minus sign; see, e.g., Eq. (6) of Zaldarriaga & Seljak (1997). The result for the Gaussian Q patch given by Eq. (A1) is shown in Fig. A1 for using $N_\ell = 36$ as the truncation level. We compare E_{glob} and B_{glob} with E and B in the range $0 < \phi < \pi$, but the calculations have been done in the full range $0 < \phi < 2\pi$.

Both E and E_{glob} as well as B and B_{glob} agree with each other and are qualitatively similar to the overall appearance of E and B seen in Fig. 3. The agreement between local and global representations shows that for a single patch in Q , the sign convention used in Durrer (2008) and Brandenburg (2019) for the global representation agrees with the local one used in (BBKMRPS) and Prabhu et al. (2020).

REFERENCES

Alton, P. B., Xilouris, E. M., Misiriotis, A., Dasyra, K. M., & Dumke, M. 2004, *A&A*, 425, 109
 Andersson, B.-G., Lazarian, A., & Vaillancourt, J. E. 2015, *ARA&A*, 53, 501
 Beck, R., Chamandy, L., Elson, E., & Blackman, E. G. 2019, *Galaxies*, 8, 4
 Beck, R., Brandenburg, A., Moss, D., Shukurov, A., & Sokoloff, D. 1996, *ARA&A*, 34, 155
 Beck, R., Berkhuijsen, E. M., Gießbübel, R., & Mulcahy, D. D. 2020, *A&A*, 633, A5
 Blackman, E. G., & Brandenburg, A. 2003, *ApJ*, 584, L99
 Bocchio, M., Bianchi, S., Hunt, L. K., & Schneider, R. 2016, *A&A*, 586, A8
 Bracco, A., Candelaresi, S., Del Sordo, F., & Brandenburg, A. 2019, *A&A*, 621, A97
 Brandenburg, A. 2015, in *Magnetic fields in diffuse media*,

ed. E. de Gouveia Dal Pino & A. Lazarian (Astrophys. Spa. Sci. Lib., Vol. 407, Springer), 529
 Brandenburg, A. 2019, *ApJ*, 883, 119
 Brandenburg, A. 2019, in *IAUS 354: Solar and Stellar Magnetic Fields: Origins and Manifestations*, ed. A. Koso- vichev, K. Strassmeier & M. Jardine (Proc. IAU Symp., Vol. 354), in press
 Brandenburg, A., & Brügggen, M. 2020, *ApJL*, submitted, arXiv:2003.14178 (BB20)
 Brandenburg, A., & Dobler, W., PENCIL CODE, <http://ui.adsabs.harvard.edu/abs/2010ascl.soft10060B> DOI:10.5281/zenodo.2315093.
 Brandenburg, A., & Stepanov, R. 2014, *ApJ*, 786, 91
 Brandenburg, A., Bracco, A., Kahniashvili, T., Mandal, S., Roper Pol, A., Petrie, G. J. D., & Singh, N. K. 2019, *ApJ*, 870, 87 (BBKMRPS)
 Brandenburg, A., Donner, K. J., Moss, D., Shukurov, A., Sokoloff, D. D., & Tuominen, I. 1992, *A&A*, 259, 453
 Brandenburg, A., Donner, K. J., Moss, D., Shukurov, A., Sokoloff, D. D., & Tuominen, I. 1993, *A&A*, 271, 36
 Brandenburg, A., Krause, F., Meinel, R., Moss, D., & Tuominen, I. 1989, *A&A*, 213, 411
 Chamandy, L., Shukurov, A., & Subramanian, K. 2015, *MNRAS*, 446, L6
 Crutcher, R. M. 2012, *ARA&A*, 50, 29
 Durrer, R. 2008, *The Cosmic Microwave Background* (Cambridge: Cambridge University Press)
 Elstner, D., Golla, G., Rüdiger, G., & Wielebinski, R. 1995, *A&AS*, 297, 77
 Fraternali, F., Sancisi, R., & Kamphuis, P. 2011, *A&A*, 531, A64
 Haas, M., Klaas, U., & Bianchi, S. 2002, *A&A*, 385, L23
 Han, J. L. 2017, *ARA&A*, 55, 111
 Hildebrand, R. H., Kirby, L., Dotson, J. L., Houde, M., & Vaillancourt, J. E. 2009, *ApJ*, 696, 567
 Horellou, C., & Fletcher, A. 2014, *MNRAS*, 441, 2049
 Hughes, T. M., Baes, M., Fritz, J., Smith, M. W. L., Parkin, T. J., et al. 2014, *A&A*, 565, A4
 Ivanova, T. S., & Ruzmaikin, A. A. 1977, *Sov. Astron.*, 21, 479
 Jones, T. J., Dowell, C. D., Lopez Rodriguez, E., Zweibel, E. G., Berthoud, M., et al. 2019, *ApJ*, 870, L9
 Junklewitz, H., & Enßlin, T. A. 2011, *A&A*, 530, A88
 Kahniashvili, T., Maravin, Y., Lavrelashvili, G., & Kosowsky, A. 2014, *PhRvD*, 90, 083004
 Kamionkowski, M., & Kovetz, E. D. 2016, *ARA&A*, 54, 227
 Kamionkowski, M., Kosowsky, A., & Stebbins, A. 1997, *PhRvL*, 78, 2058
 Krause, M. 2019, *Galaxies*, 7, 54
 Krause, F., & Rädler, K.-H. 1980, *Mean-field Magneto- hydrodynamics and Dynamo Theory* (Oxford: Pergamon Press)
 Moffatt, H. K. 1978, *Magnetic Field Generation in Elec- trically Conducting Fluids* (Cambridge: Cambridge Univ. Press)
 Moss, D., & Sokoloff, D. 2017, *A&A*, 598, A72 Galactic winds and the origin of large-scale magnetic fields
 Oosterloo, T., Fraternali, F., & Sancisi, R. 2007, *ApJ*, 134, 1019
 Oppermann, N., Junklewitz, H., Robbers, G., & Enßlin, T. A. 2011, *A&A*, 530, A89

- Parker, E. N. 1955, *ApJ*, 122, 293
Parker, E. N. 1971, *ApJ*, 163, 255
Pattle, K., & Fissel, L. 2019, *Front. Astron. Space Sci.*, 6, 1
Planck Collaboration Int. XIX. 2015, *A&A*, 576, A104
Prabhu, A., Brandenburg, A., Käpylä, M. J., & Lagg, A. 2020, *A&A*, submitted, arXiv:2001.10884
Rüdiger, G. 1978, *Astron. Nachr.*, 299, 217
Ruzmaikin, A. A., Sokoloff, D. D. & Shukurov, A. M. 1988, *Magnetic Fields of Galaxies* (Kluwer, Dordrecht)
Seljak, U., & Zaldarriaga, M. 1997, *PhRvL*, 78, 2054
Shukurov, A. 1998, *MNRAS*, 299, L21
Sokoloff, D. D., & Shukurov, A. M. 1990, *Nature*, 347, 51
Steenbeck, M., Krause, F., & Rädler, K.-H. 1966, *Z. Naturforsch.*, 21a, 369
Strickland, D. K., Heckman, T. M., Colbert, E. J. M., Hoopes, C. G., & Weaver, K. A. 2004, *ApJ*, 606, 829
Vainshtein, S. I., & Ruzmaikin, A. A. 1971, *Sov. Astron.*, 16, 365
Volegova, A. A., & Stepanov, R. A. 2010, *Sov. Phys. JETP*, 90, 637
Whaley, C. H., Irwin, J. A., Madden, S. C., Galliano, F., & Bendo, G. J. 2009, *MNRAS*, 395, 97
Zaldarriaga, M. & Seljak, U. 1997, *PhRvD*, 55, 1830